

ARTICLE

DOI: 10.1038/s42004-018-0050-y

OPEN

# In situ encapsulation of iron(0) for solar thermochemical syngas production over iron-based perovskite material

Chuande Huang<sup>1</sup>, Jian Wu<sup>1,2</sup>, You-Tao Chen<sup>3</sup>, Ming Tian<sup>1</sup>, Alexandre I. Rykov<sup>1</sup>, Baolin Hou<sup>1</sup>, Jian Lin<sup>1</sup>, Chun-Ran Chang<sup>3</sup>, Xiaoli Pan<sup>1</sup>, Junhu Wang<sup>1</sup>, Aiqin Wang<sup>1</sup> & Xiaodong Wang<sup>1</sup>

Methane-to-syngas conversion plays an important role in industrial gas-to-liquid technologies, which is commercially fulfilled by energy-intensive reforming methods. Here we present a highly selective and durable iron-based  $\text{La}_{0.6}\text{Sr}_{0.4}\text{Fe}_{0.8}\text{Al}_{0.2}\text{O}_{3-\delta}$  oxygen carrier for syngas production via a solar-driven thermochemical process. It is found that a dynamic structural transformation between the perovskite phase and a  $\text{Fe}^0$ @oxides core-shell composite occurs during redox cycling. The oxide shell, acting like a micro-membrane, avoids direct contact between methane and fresh iron(0), and prevents coke deposition. This core-shell intermediate is regenerated to the original perovskite structure either in oxygen or more importantly in  $\text{H}_2\text{O}-\text{CO}_2$  oxidant with simultaneous generation of another source of syngas. Doping with aluminium cations reduces the surface oxygen species, avoiding overoxidation of methane by decreasing oxygen vacancies in perovskite matrix. As a result, this material exhibits high stability with carbon monoxide selectivity above 95% and yielding an ideal syngas of  $\text{H}_2/\text{CO}$  ratio of 2/1.

<sup>1</sup>Dalian Institute of Chemical Physics, Chinese Academy of Sciences, 116023 Dalian, China. <sup>2</sup>College of Chemical Engineering, Northwest University, 710069 Xi'an, China. <sup>3</sup>School of Chemical Engineering and Technology, Xi'an Jiaotong University, 710049 Xi'an, China. Correspondence and requests for materials should be addressed to J.L. (email: [jianlin@dicp.ac.cn](mailto:jianlin@dicp.ac.cn)) or to C.-R.C. (email: [changcr@mail.xjtu.edu.cn](mailto:changcr@mail.xjtu.edu.cn)) or to X.W. (email: [xdwang@dicp.ac.cn](mailto:xdwang@dicp.ac.cn))

Taking full advantage of the abundant solar energy is a feasible approach to tackle the steeply increased global energy demand and mitigate the climate change induced by combustion of fossil fuels<sup>1</sup>. It is estimated that using only the solar energy from partial areas of the world's desert can in principle meet the social energy requirement<sup>2</sup>. The challenge lies in the capture and storage of the relatively diffuse and labile solar energy, which could be realized through upgrading inert molecules into high-energy fuels by solar-driven thermochemical processes<sup>3</sup>. To date, significant research has been conducted into H<sub>2</sub> and CO production by solar-driven water splitting and carbon dioxide splitting<sup>4,5</sup>. Importantly, the mixture of H<sub>2</sub> and CO, namely, syngas, could be further converted to methanol or other value-added liquid fuels by Fischer-Tropsch process, offering advantages of being easily transported and stored than gaseous fuel<sup>6</sup>. Another attractive process gaining attention for solar harvest is conversion of methane to liquid fuel via syngas intermediate, which is motivated by the increasing production capacity of natural/shale gas in recent years<sup>7,8</sup>.

In two-step solar-driven thermochemical processes (Supplementary Fig. 1), the lattice oxygen serves as an oxygen source for selective oxidation of methane promoted by solar heat energy. Subsequently, lost oxygen can be replenished using oxidants like H<sub>2</sub>O, CO<sub>2</sub>, or air with the production of H<sub>2</sub>, CO, or process heat<sup>9</sup>. Different from the well-known continuous feeding mode of steam reforming (H<sub>2</sub>/CO = 3) and dry reforming (H<sub>2</sub>/CO = 1), direct production of syngas with H<sub>2</sub>/CO ratio of 2 becomes possible in such a two-step strategy without undesirable mixing of CH<sub>4</sub> and O<sub>2</sub> as in methane partial oxidation processes<sup>10</sup>.

The key to such thermochemical processes lies in the selection of suitable oxygen carriers (OCs) to give satisfactory reactivity, selectivity, and lattice oxygen capacity for syngas production. During the past decades, various kinds of OCs, including oxides of Zn, Ce, Sn, Co, Ni, and Fe etc., have been synthesized and tested<sup>11</sup>. Hereto, particular interests are focused on the inexpensive and environmental friendly Fe-based oxides<sup>12</sup>. As early as 1993, Steinfeld et al.<sup>13</sup> have tried Fe<sub>3</sub>O<sub>4</sub> in solar-driven thermochemical process for methane-to-syngas conversion, but pure iron oxides generally showed low reduction activity and CO selectivity. Study by Kim et al.<sup>14</sup> showed that the production of syngas prevailed over the total oxidation to CO<sub>2</sub> only when more than 50% of Fe<sub>3</sub>O<sub>4</sub> was converted to FeO. Although further reduction of FeO to metallic Fe<sup>0</sup> is favorable for higher CO/CO<sub>2</sub> ratio and oxygen capacity, serious coke deposition would occur due to methane decomposition over Fe<sup>0</sup>, leading to increased H<sub>2</sub>/CO ratio and lower CO selectivity. Modification through structural or electronic promoters has been explored to improve the overall performance. Müller et al.<sup>15</sup> demonstrated that Cu-modified Fe<sub>2</sub>O<sub>3</sub>/MgAl<sub>2</sub>O<sub>4</sub> composite can result in partial coverage of reduced Fe<sup>0</sup> with Cu, leading to better reactivity and lowered rates of carbon deposition. Li et al.<sup>16</sup> reported that the incorporation of Fe–Ce mixed oxide can increase the CO selectivity to ca. 85%, which was attributed the strong interaction between reduced iron and cerium oxides. Neal et al.<sup>17</sup> fabricated a Fe<sub>2</sub>O<sub>3</sub>@La<sub>0.8</sub>Sr<sub>0.2</sub>FeO<sub>3-δ</sub> composite and found that Fe<sub>2</sub>O<sub>3</sub> could be reduced to Fe<sup>0</sup>/FeO with no coke deposition due to the good ionic-electronic conductivity of the outer perovskite layer. However, although much effort has been made, it was found that traditional modification of iron oxides generally led to relatively limited CO selectivity before coke formation.

From the above studies, we conclude that the performance of Fe-based oxides could be greatly altered by catalyst structure engineering. Perovskite (ABO<sub>3</sub>) oxides are an important class of functional materials, the structure of which can be significantly modulated by even slight substitution of A or B site cations<sup>18</sup>. For production of syngas, the single phase LaFeO<sub>3</sub> perovskite showed

significantly enhanced reactivity toward methane conversion than iron oxides<sup>19</sup>. However, Fe cations can be reduced only from Fe<sup>3+</sup> to Fe<sup>2+</sup> in methane atmosphere and further reduction would induce coke deposition<sup>20</sup>. Comparatively, when the A site of La in LaFeO<sub>3</sub> was partially substituted by Sr to mitigate coke formation, the syngas selectivity was reduced due to generation of oxygen vacancies associated with more surface adsorbed oxygen<sup>21</sup>. These studies suggest a “seesaw” effect for Fe-based perovskite OCs in selective oxidation of methane, between Fe valence variation to supply more lattice oxygen, and its performance (e.g., reactivity, selectivity, and stability).

Here, we report a perovskite oxide with formula La<sub>0.6</sub>Sr<sub>0.4</sub>Fe<sub>0.8</sub>Al<sub>0.2</sub>O<sub>3-δ</sub> for selective oxidation of methane to syngas. This perovskite with A and B sites substituted by Sr and Al cations not only reduces the surface active oxygen species for CH<sub>4</sub> over-oxidation but also facilitates in situ encapsulation of Fe<sup>0</sup>, originating from deep reduction of Fe<sup>4+</sup> with the formation of Fe<sup>0</sup>@oxides composite. This core-shell structure switches off the pathway for Fe<sup>0</sup> to catalyze methane pyrolysis, and also favors reformation of the original perovskite phase either in strong O<sub>2</sub> or soft H<sub>2</sub>O–CO<sub>2</sub> oxidant. Consequently, this material exhibits redox stability in the harsh thermochemical process and syngas selectivity of above 95% with H<sub>2</sub>/CO of 2 and no coke deposition.

## Results

**Structural characterization.** The XRD patterns of as-prepared LaFeO<sub>3</sub> and La<sub>0.6</sub>Sr<sub>0.4</sub>Fe<sub>1-x</sub>Al<sub>x</sub>O<sub>3-δ</sub> (denoted as LSF6410 and LSAF6428 for *x* = 0 and 0.2 samples, respectively) oxides indicate that all samples show pure perovskite phase and no impurities such as SrCO<sub>3</sub>, La<sub>2</sub>O<sub>3</sub>, and Al<sub>2</sub>O<sub>3</sub> are detected (Supplementary Fig. 2). Some basic physical parameters of the fresh catalysts are listed in Supplementary Table 1. Figure 1a presents the normalized Fe K-edge XANES spectra of different catalysts at room temperature. It shows that the intensity of white line (W: 1s → 4p transition) at ca. 7130 eV notably decreases when La cations in LaFeO<sub>3</sub> were partially substituted by Sr, which is further lowered after doping of Al (i.e., LSAF6428). Correspondingly, the absorption edge gradually shifts to higher energies accompanied with decrease of white line intensity. These results indicate that the average valence state of Fe cations increases after introduction of Sr and Al in LaFeO<sub>3</sub> matrix to maintain charge balance<sup>22</sup>. In other words, Fe<sup>4+</sup> cations with higher valence state (Fe<sup>3+</sup> in LaFeO<sub>3</sub>) exist in LSF6410, the content of which is further improved after Al doping for LSAF6428. For the pre-edge feature (P) attributed to 1s → 3d transition, it is generally accepted that the intensity would increase with Fe valence state and stronger mixing between Fe 3d and O 2p states<sup>23</sup>. A more intense of P for LSF6410 than that for LaFeO<sub>3</sub> is observed in Fig. 1, which is in agreement with the higher average valence state of Fe cations in LSF6410. However, further doping of Al results in the slightly lower intensity, which is contrary to increased Fe valence state for LSAF6428 than that for LSF6410. These results suggest that the doping of Al could weaken the admixing of O-p orbital.

The chemical state of Fe was further investigated by <sup>57</sup>Fe Mössbauer spectroscopy (Fig. 1b) and the corresponding fitted parameters are listed in Supplementary Table 2. The Mössbauer spectra of LaFeO<sub>3</sub> show a typical sextet with IS (isomer shift) = 0.36 mm/s, QS (quadrupole splitting) = 0.00 mm/s, and H (hyperfine field) = 51.7 T, which is characteristic of Fe<sup>3+</sup> cations with antiferromagnetic property<sup>24</sup>. However, only a singlet with wide absorption wings is observed for LSF6410, indicating that the magnetic ordering temperature of this material is around room temperature<sup>25</sup>. The IS values for both Fe species are fitted to 0.20 mm/s, between that for Fe<sup>4+</sup> (~ 0.0 mm/s) and Fe<sup>3+</sup> (~ 0.36 mm/s), which suggests the existence of Fe<sup>3+↔4+</sup> mixed

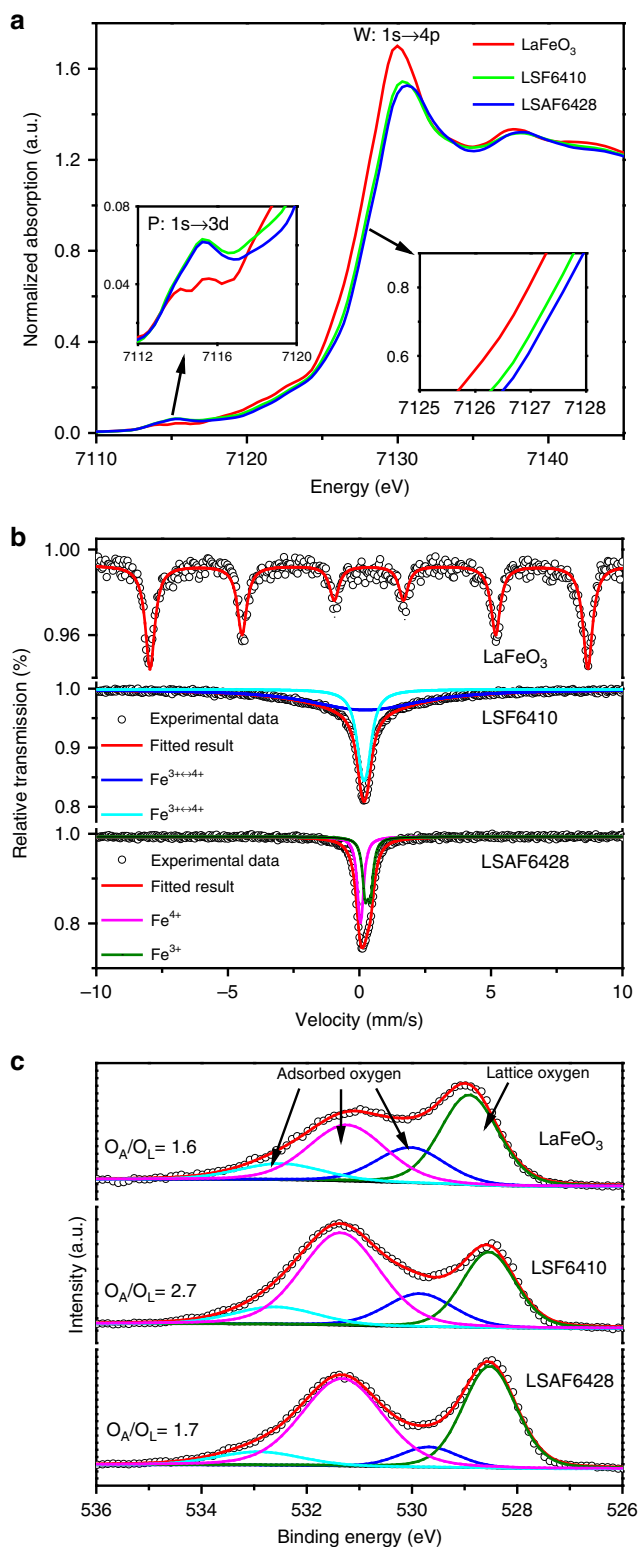


**Fig. 1** Structural characterization of as-prepared catalysts. **a** Normalized Fe K-edge XANES spectra, **b** room temperature  $^{57}\text{Fe}$  Mössbauer spectra, and **c** XPS results of O1s peak of  $\text{LaFeO}_3$ , LSF6410, and LSAF6428 catalysts. For inset figure of **a**, P and W show the pre-edge and white line features

valence state induced by rapid charge hopping at room temperature<sup>26</sup>. Combining the low temperature (77 K) Mössbauer analysis (Supplementary Fig. 3 and Supplementary Table 2), the average valence of Fe cations was calculated to be 3.36. Further introduction

of Al cations leads to totally paramagnetic property of LSAF6428 material with further increase of Fe valence, in which the proportion of  $\text{Fe}^{4+}$  and  $\text{Fe}^{3+}$  is 49 and 51%, respectively, as shown in Supplementary Table 2. According to the charge balance principle, the amount of oxygen vacancies ( $\delta$ ) is determined to be 0.020 and 0.005 for LSF6410 and LSAF6428, respectively, indicating that partial substitution of Fe by Al can significantly suppress formation of oxygen vacancies in the perovskite matrix.

Figure 1c shows the O1s core-level photoemission spectra. Two strong features could be observed for the three as-prepared catalysts. The peak at lower binding energy (BE) of ca. 528.5 eV is assigned to the lattice oxygen ( $\text{O}_L$ ) while the broad shoulder lying in the region of 530.0–533.0 eV is attributed to the surface adsorbed oxygen ( $\text{O}_A$ )<sup>27</sup>. By deconvoluting this broad peak, three different oxygen species are identified: the one with lowest BE (ca. 529.7 eV) is ascribed to  $\text{O}_2^{2-}/\text{O}^-$ , the one at BE of ca. 531.3 eV is assigned to oxygen in the form of hydroxyl ( $\text{OH}^-$ ) and carbonate ( $\text{CO}_3^{2-}$ ), and the peak with highest BE value (ca. 532.9 eV) is associated with molecular water adsorbed on the surface<sup>28,29</sup>. It is well accepted that the  $\text{O}_A/\text{O}_L$  ratio is proportional to the concentration of oxygen vacancies in the catalysts. According to the fitted results, this ratio increases from 1.6 for  $\text{LaFeO}_3$  to 2.7 for LSF6410, while decreases in turn to 1.7 with further doping of Al. These results further confirmed that doping of Sr would induce formation of oxygen vacancies while introduction of Al shows the opposite effect.

**Catalytic performance for the production of syngas.** Figure 2 displays the performance of Sr/Al-doped  $\text{LaFeO}_3$  catalysts in selective conversion of methane to syngas. The CO selectivity over  $\text{LaFeO}_3$  (Fig. 2a) is 93% with  $\text{H}_2/\text{CO}$  ratio (Fig. 2b) slightly higher than 2 in the first cycle, which is similar to the previous reports<sup>30</sup>. It decreases gradually with further cycle numbers. As for LSF6410 sample, this value is initially lower of 90% and decreases to 85% after 20 cycles. In contrast, the additional dopant of Al could improve the CO selectivity, which reaches ~95% within 20 cycles with a steady  $\text{H}_2/\text{CO}$  ratio of 2/1 over LSAF6428. Figure 2c shows the amount of convertible lattice oxygen, an important factor in selective oxidation of methane. LSAF6428 donates the highest amount of ~2.8 mmol  $\text{O}/\text{g}_{\text{cat}}$  in the first cycle, which is much higher than that for LSF6410 (~2.1 mmol  $\text{O}/\text{g}_{\text{cat}}$ ) and  $\text{LaFeO}_3$  (~1.6 mmol  $\text{O}/\text{g}_{\text{cat}}$ ). With increasing the cycle numbers, this value slightly changes but still follows the order of LSAF6428 > LSF6410 >  $\text{LaFeO}_3$ , which is in line with conversion of  $\text{CH}_4$  (Fig. 2d). Clearly, the dopant of both Sr and Al cations plays an important role in improving the performance of this OC in terms of the excellent selectivity to CO and stability.

The catalytic performances of LSAF6428 and the representative oxides reported previously are listed in Table 1. Typically, the NiO-based catalysts exhibit acceptable CO selectivity (~90%) as shown in Entries 4 and 5, but large amount of  $\text{H}_2\text{O}$  is required in the feedstock to suppress carbon deposition and overoxidation of methane, leading to  $\text{H}_2/\text{CO}$  ratio much higher than 2<sup>31,32</sup>.  $\text{LaFeO}_3$  exhibits an initial CO selectivity of ~96% under optimized conditions as shown in Entry 8, but the quantity of  $\text{CO}_2$  increases and the deactivation is observed after only 7 cycles due to sintering of material<sup>30,33,34</sup>. The recently developed iron-titanium composite oxide (Entry 10) shows steady activity for several hours in the moving bed reactor<sup>35</sup>. However, a higher temperature of 975–1000 °C is needed to reach the 90% CO selectivity. In contrast, LSAF6428 catalyst presents almost the best CO selectivity with the desired  $\text{H}_2/\text{CO}$  ratio of 2 at 900 °C (Entry 1). Even at more cycling numbers of 100, a CO selectivity of 92% still remains without changes for  $\text{H}_2/\text{CO}$  ratio, indicating a good

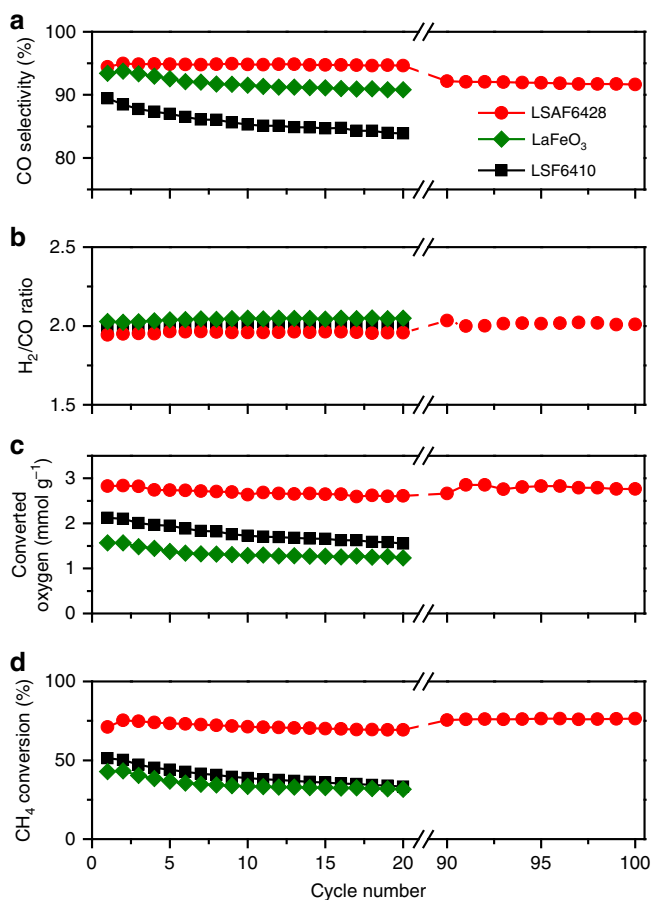


**Fig. 2** Methane-to-syngas performance over different catalysts. **a** Comparison of CO selectivity, **b** H<sub>2</sub>/CO ratio, **c** the amount of convertible lattice oxygen, and **d** CH<sub>4</sub> conversion in the selective oxidation of CH<sub>4</sub> over different catalysts with cycle number of alternative CH<sub>4</sub> and O<sub>2</sub> at 900 °C

stability of this catalyst for long-term syngas production. When decreasing the reaction temperature to 800 °C, it still exhibits a good CO selectivity of 93% and ideal H<sub>2</sub>/CO ratio as shown in Entry 2. It is evident that LSAF6428 is among the best materials so far for the selective conversion of methane to syngas with an extraordinary stability<sup>36,37</sup>.

The versatility of OCs using different types of oxidants is another parameter for the potential application. Figure 3 and Entry 3 of Table 1 display the performance results with alternative soft oxidant of CO<sub>2</sub>-H<sub>2</sub>O mixture. As seen, the H<sub>2</sub>/CO ratio still remains a steady value of 2.0 with a CO selectivity of ~95% in the selective oxidation of methane. The CO<sub>2</sub> and H<sub>2</sub>O conversion (Fig. 3b) reach as high as 61 and 64%, respectively, which is even higher than the theoretical carbon dioxide or water splitting efficiency on iron oxides (Supplementary Table 3). More importantly, during the fill of lattice oxygen with H<sub>2</sub>O and CO<sub>2</sub>, valuable syngas with H<sub>2</sub>/CO ratio of ~2 is generated. The above results indicate the good structure reversibility of LSAF6428 with strong or soft oxidant and two sources of syngas can be obtained by changing the oxidant from O<sub>2</sub> to CO<sub>2</sub> + H<sub>2</sub>O.

**The factors for the high performance of LSAF6428.** The above results show that LSAF6428 exhibit good overall performance (activity, selectivity, and stability) for the long-term redox reactions to produce syngas either with strong O<sub>2</sub> or soft H<sub>2</sub>O/CO<sub>2</sub> as oxidants. The structure analysis (Supplementary Fig. 4) shows

that an impure phase attributed to La<sub>2</sub>O<sub>3</sub> appears for spent LaFeO<sub>3</sub>, indicating that the single perovskite phase can not be easily regenerated after 20 cycles. In contrast, the Sr/Al-doped materials all maintain the same perovskite structure as the fresh sample, demonstrating the excellent structural stability. The typical SEM images of the spent samples are given in Supplementary Fig. 5. It is clearly noticed that the particle size of LaFeO<sub>3</sub> and LSF6410 notably increase after 20 redox cycles. However, negligible changes of particle size and surface area are observed for LSAF6428. The above results suggest that co-doping of Sr and Al in LaFeO<sub>3</sub> could improve the structural stability and the sintering resistance during long-term redox reactions.

The reactivity of lattice oxygen in the selective oxidation of CH<sub>4</sub> strongly depends on the chemical state of transition metals<sup>17</sup>. Thus, CH<sub>4</sub> pulse reaction was conducted to gain insight into the gradual evolution of the methane-to-syngas performance with extraction of lattice oxygen from LSAF6428 material. As shown in Fig. 4a, methane is mainly converted to CO<sub>2</sub> at the very beginning of selective oxidation reaction, leading to low CO selectivity of only 35% (Fig. 4b). However, the subsequent pulse reaction results in CO selectivity up to above 95% (Fig. 4b). It is accepted that two types of oxygen species, i.e., active surface adsorbed oxygen and selective lattice oxygen, co-exist in the OCs<sup>38</sup>. The first pulse of CH<sub>4</sub> consumed almost all of the surface oxygen on LSAF6428, which contributes to the total combustion of methane to CO<sub>2</sub> and H<sub>2</sub>O while the following results in the production of syngas. According to the XANES (Fig. 1a) and <sup>57</sup>Fe Mössbauer spectroscopy (Fig. 1b) analysis, doping of Al cations can facilitate the formation of Fe<sup>4+</sup> cations and lead to declined oxygen vacancies with notably improved CO selectivity, which may be caused by the strong Al-O interaction<sup>39,40</sup>. The absolute oxygen vacancy formation energy ( $E_{\text{vac}}$ ) was calculated with the equation  $E_{\text{vac}} = E_{\text{defect-surface}} + 1/2 E_{\text{O}_2} - E_{\text{surface}}$  based on the structure of (110) and (012) plane. Two kinds of oxygen vacancy (Supplementary Fig. 6) possibly formed on LSAF6428, i.e., oxygen vacancy neighboring to Fe site (denoted as Fe-O<sub>vac</sub>) and oxygen vacancy neighboring to Al site (denoted as Al-O<sub>vac</sub>). DFT calculations show that the  $E_{\text{vac}}$  of Fe-O<sub>vac</sub> is 1.72 eV and 0.21 eV lower than the  $E_{\text{vac}}$  of Al-O<sub>vac</sub> on (110) and (012), respectively, indicating that Al cations could benefit the stability of surface oxygen and suppress the formation of oxygen vacancies. Combined with the reaction results (Fig. 2), one can conclude that the reduced oxygen vacancies induced by Al introduction results in decrease of active surface adsorbed oxygen (Fig. 1c). Thus, an initial decline of CH<sub>4</sub> conversion is observed from 70% (1st pulse) to 53% (2nd pulse). However, this conversion gradually increases to 85% (25th pulse) afterward, indicating that partial reduction of this perovskite material would contribute to enhanced reactivity. As for the H<sub>2</sub>/CO ratio, it keeps a constant value of ~2.0 from 3rd to 25th pulse, suggesting a high lattice oxygen transferring ability from the body of LSAF6428 particle to its surface, which effectively inhibits the coke deposition by methane decomposition<sup>19</sup>. The above results give a clue that the Fe chemical state evolution induced by extraction of oxygen greatly alters the performance of LSAF6428 material.

The evolution of Fe chemical state with CH<sub>4</sub> pulses was tracked by Mössbauer spectroscopy. As seen from Fig. 5a, the doublets of as-prepared LSAF6428 (Fig. 1b) is transformed to overlap of sextets and doublets due to loss of lattice oxygen even after slight reduction by CH<sub>4</sub>. The fitted parameters (Supplementary Table 4) show that Fe<sup>0</sup> species (5%) are already generated after only five CH<sub>4</sub> pulses accompanied with the formation of LaSrFe<sub>1-x</sub>Al<sub>x</sub>O<sub>4</sub> double perovskite oxides. However, the characteristic peaks of Fe<sup>0</sup> phase are not identified until 10th pulse from the XRD analysis (Fig. 5b), which may be attributed to its high dispersion or low degree of crystallinity at the initial period of reaction. Combined

**Table 1 Comparison of methane-to-syngas performance over different catalysts**

Entry	Material	T (°C)	CO sel. (%)	H <sub>2</sub> /CO ratio	Coke (mmol g <sup>-1</sup> )	Reaction cycles <sup>a</sup>	Ref.
1	LSAF6428 <sup>b</sup>	900	95	2.0	0	100	This work
2	LSAF6428	800	93	2.0	0	20	This work
3	LSAF6428 <sup>c</sup>	900	95	2.0	0.03	20	This work
4	NiO/SiO <sub>2</sub> <sup>d</sup>	800	80	3.4	N	FB	31
5	NiO/MgO-ZrO <sub>2</sub> <sup>e</sup>	940	89	2.2	N	FB	32
6	Rh <sub>2</sub> O <sub>3</sub> -Fe <sub>2</sub> O <sub>3</sub> /Y <sub>2</sub> O <sub>3</sub>	800	56	2.2	0.08	1	33
7	CeO <sub>2</sub>	850	92	1.89	N	1	16
8	LaFeO <sub>3</sub> <sup>f</sup>	900	96	1.93	N	7	30
9	Fe <sub>2</sub> O <sub>3</sub> -La <sub>0.8</sub> Sr <sub>0.2</sub> FeO <sub>3</sub> <sup>g</sup>	900	68 <sup>h</sup>	1.9	0.18	5	34
10	Fe <sub>2</sub> TiO <sub>5</sub>	975	92	1.97	1.5% of CH <sub>4</sub>	MB	35
11	BaMn <sub>0.5</sub> Fe <sub>0.5</sub> O <sub>3-δ</sub> <sup>i</sup>	900	90	2.1	<6% of CH <sub>4</sub>	18	36
12	SrFeO <sub>3-δ</sub> -CaO <sup>j</sup>	900	96	2	N	16	37

N means the data is not given in the reference; FB and MB represent fluidized bed and moving bed, respectively

<sup>a</sup>The reaction was conducted on fixed bed reactor except the ones with notes of FB and MB

<sup>b</sup>Average value of the results from 1st to 20th cycle

<sup>c</sup>2.5% CO<sub>2</sub> + 5% H<sub>2</sub>O was used as oxidant

<sup>d</sup>50% H<sub>2</sub>O was added to the feedstock

<sup>e</sup>30% H<sub>2</sub>O was added to the feedstock

<sup>f</sup>The reaction result of 7th cycle

<sup>g</sup>Result of 5th cycle with H<sub>2</sub>O/N<sub>2</sub> as oxidant

<sup>h</sup>This value shows the syngas yield

<sup>i</sup>The performance results were the average value of last five cycles and H<sub>2</sub>O in N<sub>2</sub> was used as oxidant

<sup>j</sup>Results after 2nd cycle and CO<sub>2</sub> in Ar was used as oxidant

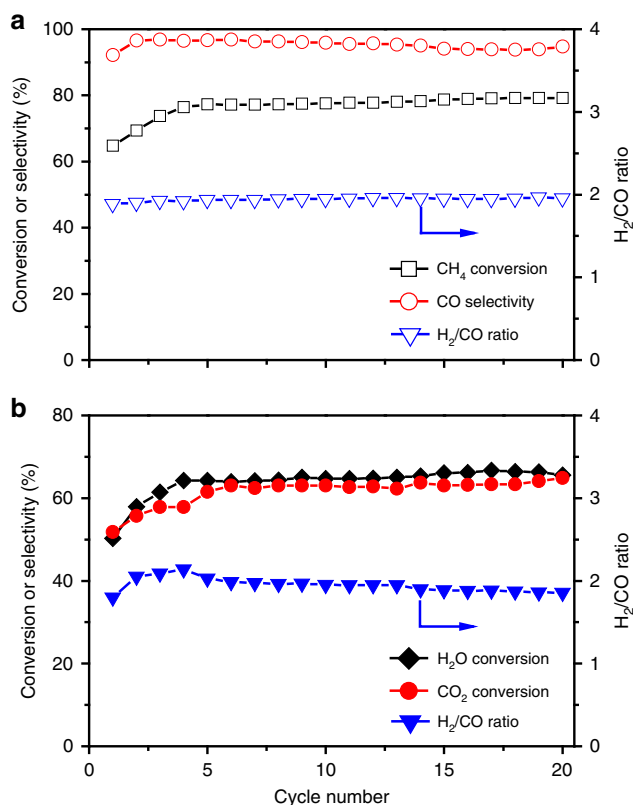


**Fig. 3** Performance of LSAF6428 using CO<sub>2</sub>-H<sub>2</sub>O mixture as oxidant at 900 °C. **a** CH<sub>4</sub> conversion, CO selectivity, and H<sub>2</sub>/CO ratio in the selective oxidation CH<sub>4</sub> step and **b** corresponding H<sub>2</sub>O, CO<sub>2</sub> conversion, and H<sub>2</sub>/CO ratio in reoxidation step

with the reaction production analysis (Fig. 4), the generation of metallic Fe<sup>0</sup> and double perovskite LaSrFe<sub>1-x</sub>Al<sub>x</sub>O<sub>4</sub>, induced by loss of lattice oxygen, would improve the reactivity of the catalyst. With continuous injection of CH<sub>4</sub>, 39% of Fe cations are reduced to Fe<sup>0</sup> after 25th pulses with generation of comparative amount of

LaSrFe<sub>1-x</sub>Al<sub>x</sub>O<sub>4</sub> (39%). Combined with the gas composition analysis (Fig. 4), it was calculated that deep reduction of these Fe cations to Fe<sup>0</sup> could supply ca. 2.7 mmol O/g<sub>cat</sub> for methane oxidation (Supplementary Fig. 7). As for LSAF6428 reduced in fixed bed reaction (5% CH<sub>4</sub>/He for 5 min at 900 °C), the ratio of metallic Fe<sup>0</sup> phase reaches 44% (Supplementary Fig. 8). Other Fe phases like Fe<sub>3</sub>O<sub>4</sub> and FeO are not detected in all these samples. This result suggests that the LSAF6428 perovskite catalyst is prone to transform into Fe<sup>0</sup> and double perovskite phase spontaneously under highly reductive atmosphere (CH<sub>4</sub>, H<sub>2</sub>, and CO).

It is well accepted that metallic Fe<sup>0</sup> are favorable for cracking of methane to induce coke deposition<sup>41</sup>, which is another issue that lowers the CO selectivity and leads to increased H<sub>2</sub>/CO ratio much higher than 2. However, it is surprising that there is no coke deposition on LSAF6428 catalyst despite the fact that the percentage of metallic Fe<sup>0</sup> reaches as high as 44%. XPS results in Supplementary Fig. 9 shows that only Fe<sup>3+</sup> species are found on the surface of the reduced catalyst. These results imply that the metallic Fe<sup>0</sup> might be encapsulated by a layer of oxides. HRTEM characterization was conducted to confirm the local structure of reduced LSAF6428 catalyst. As shown with different magnification images in Fig. 6a and Supplementary Fig. 10, all metallic Fe<sup>0</sup> with various sizes are covered by oxide layers. This phenomenon is more clearly illustrated by detecting the environment around a particle with energy dispersive spectroscopy (EDS) mapping. As shown in Fig. 6c-h, the area enriched with Fe species has relatively low concentration of La, Sr, Al, O elements. The quantitative line scan crossing a particle and dot scan at sites in the margin and center of a particle (Supplementary Fig. 11) show that the atomic percentage of Fe (in all metal cations) in the center reaches 65%, much higher than the theoretical 40% in LSAF6428. Meanwhile, the mole ratio of oxygen/metal cations (La-Sr-Fe-Al) obviously decreases from 1.5 to 0.7 (mole ratio of O/Fe in FeO is 1), which further suggest the presence of Fe<sup>0</sup> species in the center of a particle. In contrast, the proportion of Al in the margin increases from theoretical 10 to ~15% (Supplementary Fig. 11B). Also, the oxide in the margin exhibits lattice fringes with spacing of 2.76 and 2.81 Å (Fig. 6b), which can be ascribed to the (013), (-110), and (103) planes of LaSrFe<sub>1-x</sub>Al<sub>x</sub>O<sub>4</sub>.

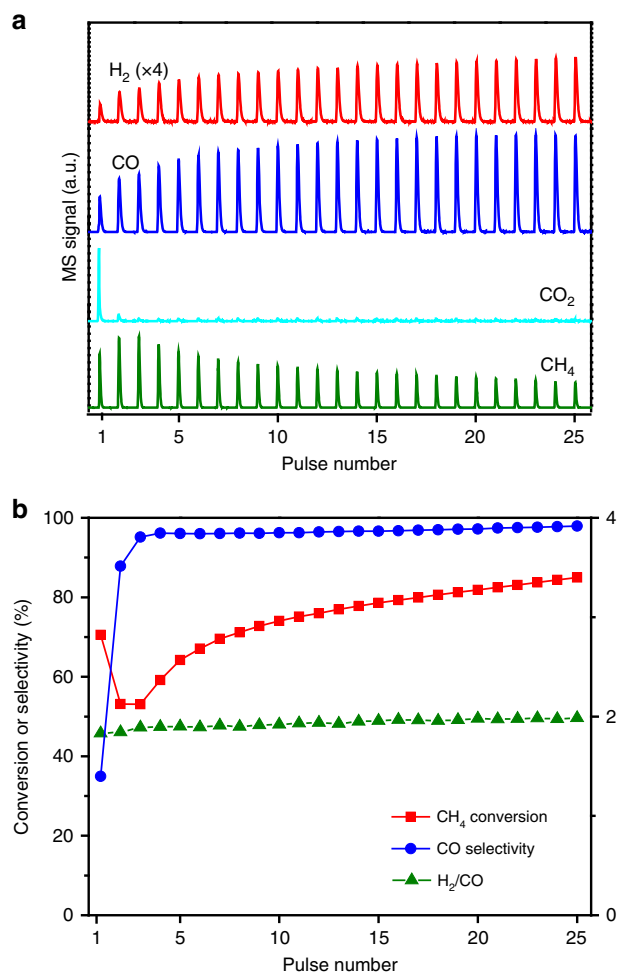


**Fig. 4** CH<sub>4</sub> pulse reactions over LSAF6428 at 900 °C. **a** Gas composition and **b** corresponding CH<sub>4</sub> conversion, CO selectivity, and H<sub>2</sub>/CO ratio

$\delta$  oxide. All the above results unequivocally indicate that Fe<sup>0</sup> is dynamically formed and grows inside the particle with the cover of Al-rich perovskite oxides.

The encapsulation of metals by oxides in reducing atmosphere, known as strong metal-support interactions (SMSI), has already been identified in various systems like Pt/TiO<sub>2</sub> and Au/ZnO<sup>42,43</sup>. As for perovskite oxides, Ramesh et al.<sup>44</sup> also found that when La<sub>0.5</sub>Sr<sub>0.5</sub>FeO<sub>3</sub> target was used to grow films on SrTiO<sub>3</sub> substrate in vacuum by pulsed laser deposition method, Fe<sup>0</sup> covered by LaSrFeO<sub>4</sub> was obtained. The encapsulation of Fe<sup>0</sup> by oxide layer of LaSrFe<sub>1-x</sub>Al<sub>x</sub>O<sub>4- $\delta$</sub>  may be induced by the highly reductive atmosphere, leading to SMSI state of the reduced catalyst. Under such circumstances, the channels for direct contact between metallic Fe<sup>0</sup> and methane are switched off. This layer of LaSrFe<sub>1-x</sub>Al<sub>x</sub>O<sub>4</sub> oxides works like a membrane<sup>45</sup>, which exhibits good lattice oxygen conductivity and can continuously devote lattice oxygen for the methane-to-syngas reaction. Thus, almost all Fe<sup>4+</sup> cations could be deeply reduced to Fe<sup>0</sup> while carbon deposition is avoided and a high CO selectivity is reached with favorable H<sub>2</sub>/CO ratio of 2. The CH<sub>4</sub> pulse reaction (Fig. 4) also shows that the methane conversion is notably improved after the formation of Fe<sup>0</sup>@LaSrFe<sub>1-x</sub>Al<sub>x</sub>O<sub>4</sub>, indicating that such core-shell intermediate is capable to selectively convert CH<sub>4</sub> to syngas more efficiently than LSAF6428. The corresponding XPS analysis (Supplementary Fig. 12A) shows that only Fe<sup>3+</sup> cations exist while no Fe<sup>0</sup> signals was observed even after 25th

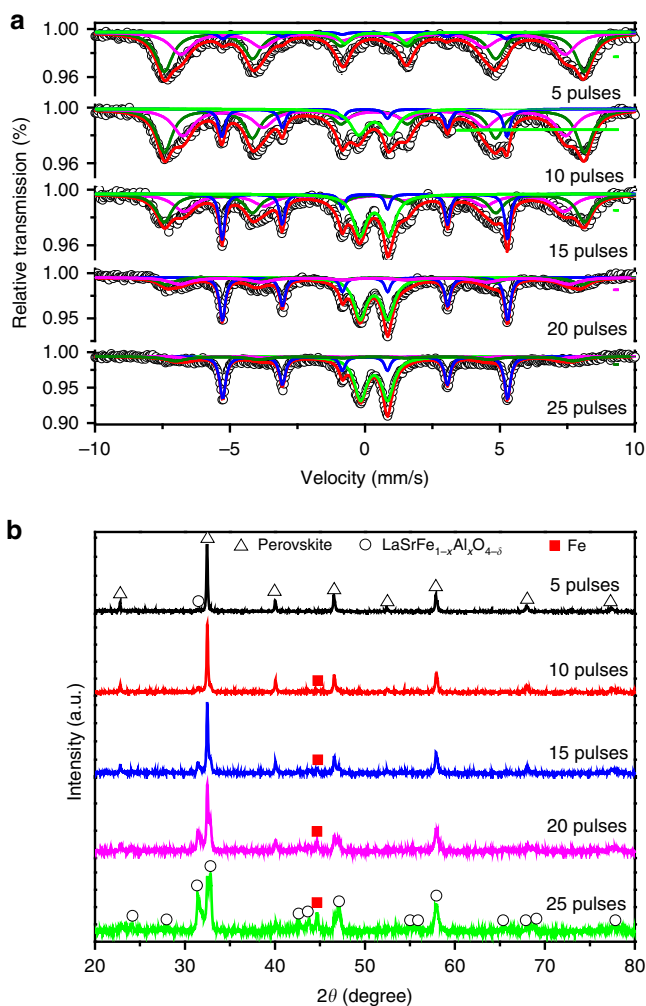


**Fig. 5** Structure evolution of LSAF6428 during CH<sub>4</sub> pulse reactions. **a** Room temperature <sup>57</sup>Fe Mössbauer spectra and **b** XRD patterns after reactions of different CH<sub>4</sub> pulses

pulses. These results indicate that Fe<sup>0</sup> species, formed initially at the surface, can be quickly covered by oxide layer containing Fe<sup>3+</sup> cations as soon as they emerge. The surface composition analysis (Supplementary Fig. 12B) shows that the O<sub>A</sub>/O<sub>L</sub> ratio increases with CH<sub>4</sub> pulses, which means that the concentration of oxygen vacancies at the surface rose with the reduction process. Combined the above results, it suggests that undercoordinated iron species may play the main role in methane activation. Besides, it was reported that the oxide shell with double perovskite structure exhibited higher surface oxygen exchange rate and oxygen mobility than pure perovskite oxide<sup>46</sup>, which also contributes to the increased reactivity. In a word, the in situ encapsulation of metallic Fe<sup>0</sup> by oxide layer during methane-to-syngas process can not only improve the CO selectivity by prohibiting carbon deposition but also notably promote the syngas production efficiency.

The durability of OCs with excellent structural reversibility is of great importance for long-term redox reactions. For Fe-based perovskite OCs, the perovskite structure would collapse and transform to oxide composite (e.g., La<sub>2</sub>O<sub>3</sub>, FeO<sub>x</sub>, and LaSrFeO<sub>4</sub>) due to loss of lattice oxygen<sup>17,19</sup>. Afterward, the oxygen is replenished in oxidative atmosphere and the perovskite structure is regenerated by solid reaction. When the reduced LSAF6428 is exposed to oxygen atmosphere, it is noticed that

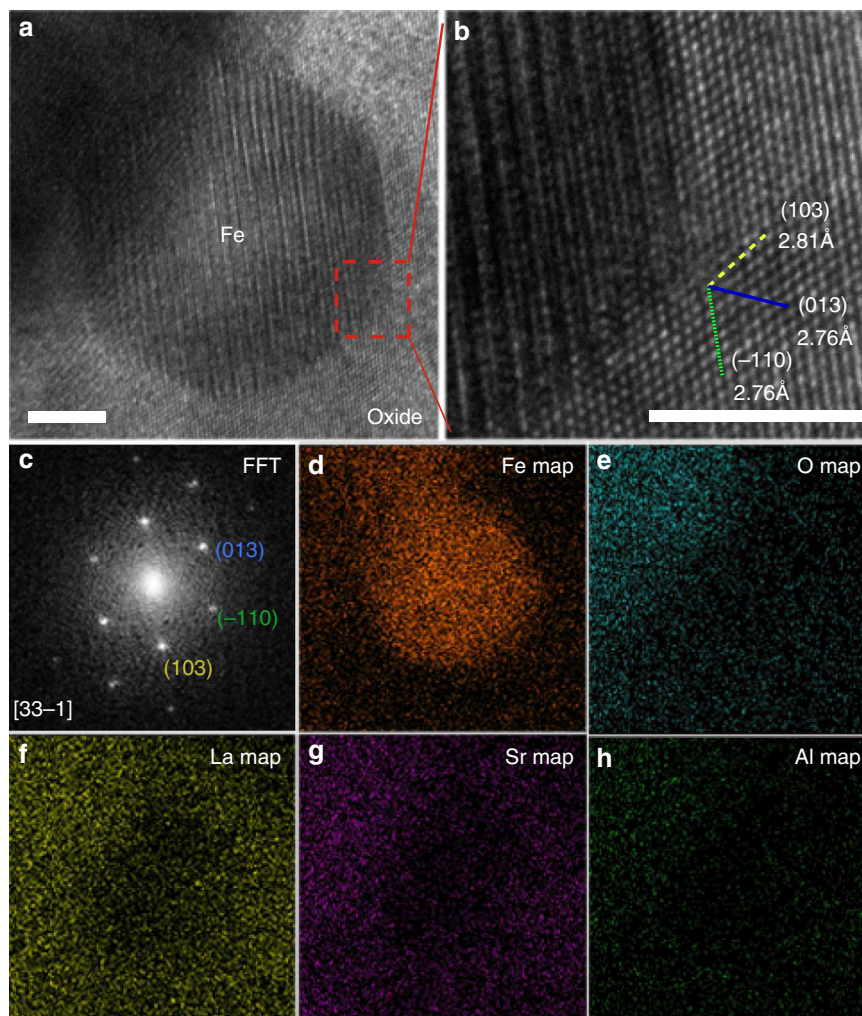


**Fig. 6** Direct evidence of  $\text{Fe}^0$  encapsulated by oxides. **a** HRTEM image of a typical metallic  $\text{Fe}^0$  particle nucleated inside membrane of oxides. **b** An enlarged district of image **a** and **c** corresponding FFT result. **d** **e** O, **f** La, **g** Sr, and **h** Al EDS maps of the same region of image **a**. Scale bars 5 nm

the metallic  $\text{Fe}^0$  can never be detected after oxidation for 0.5 min and the single perovskite structure is completely regenerated after only 2 min (Supplementary Fig. 13), which indicates that regeneration of the perovskite phase in oxygen is much faster than the decomposition rate in methane reduction process (5 min). During the regeneration process, the oxide layer can deliver oxygen to inner  $\text{Fe}^0$  coupled with the oxidation of  $\text{Fe}^0$  species in oxidizing atmosphere, while the confined Fe species in the core area of particle re-enter the perovskite lattice. Various studies on the kinetics of solid reaction showed that the fabrication of core-shell structure could accelerate the formation of perovskite, since the contact area of the reactants is normally larger while the ion diffusion distance is decreased<sup>47,48</sup>. For  $\text{LaFeO}_3$ ,  $\text{La}_2\text{O}_3$  phase appeared obviously after 20 cycles as shown in Supplementary Fig. 5, which indicates that the reduced composite without core-shell structure can not be easily transformed to original pure perovskite phase. In contrast, the in situ formation of core-shell structure for LSAF6428 in methane atmosphere is helpful for the regeneration of perovskite structure. Actually, the catalyst structure (Supplementary Fig. 14A) could be well recovered even after 100 redox cycles, accompanied by recovery of the Fe valence state (Supplementary Fig. 14B), which shows the outstanding redox stability of LSAF6428 material.

## Discussion

Based on the above analysis, the structure evolution of LSAF6428 catalyst during the methane-to-syngas process can be summarized in Fig. 7. At the very beginning of the reaction cycle, methane is mainly converted to  $\text{CO}_2$  and  $\text{H}_2\text{O}$  with rapid consumption of the active surface adsorbed oxygen, leading to low CO selectivity. Soon afterward, the selective lattice oxygen is used for partial oxidation of methane to produce syngas with ideal  $\text{H}_2/\text{CO}$  ratio of 2 and the coordination unsaturated Fe cations can improve the conversion of methane. At the same time, the perovskite structure gradually collapsed and transformed to composite of metallic  $\text{Fe}^0$  species and  $\text{LaSrFe}_{1-x}\text{Al}_x\text{O}_4$  oxides due to loss of lattice oxygen. The SMSI between  $\text{Fe}^0$  and  $\text{LaSrFe}_{1-x}\text{Al}_x\text{O}_4$  could induce the encapsulation of  $\text{Fe}^0$  by oxide with formation of core-shell structure. Therefore, the contact tunnel for  $\text{Fe}^0$ - $\text{CH}_4$  direct contact is switched off, which greatly enhances the methane-to-syngas reactivity, suppresses the coke deposition and enables deep reduction of  $\text{Fe}^{3+/4+}$  cations to  $\text{Fe}^0$ . Such core-shell intermediate can be easily regenerated to original perovskite phase by either strong oxidant of  $\text{O}_2$  or soft ones of  $\text{H}_2\text{O}$ - $\text{CO}_2$ , leading to good redox stability of this material. Importantly, when  $\text{H}_2\text{O}$ - $\text{CO}_2$  was applied for oxidant, another new source of syngas was produced.

In summary, a perovskite-type  $\text{La}_{0.6}\text{Sr}_{0.4}\text{Fe}_{0.8}\text{Al}_{0.2}\text{O}_{3-\delta}$  catalyst has been developed for the selective oxidation of  $\text{CH}_4$  to syngas using

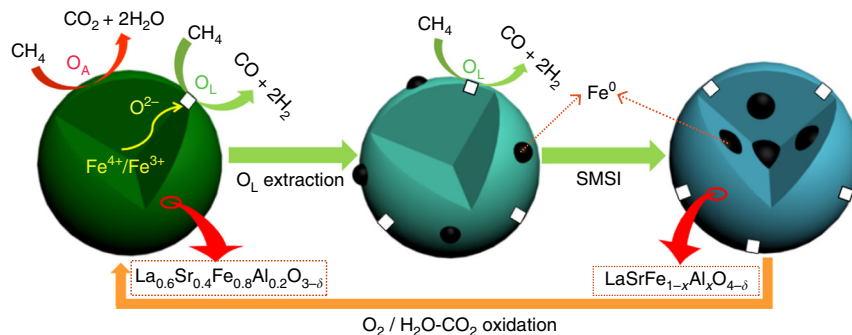


**Fig. 7** Proposed structural evolution over LSAF6428 for the selective oxidation of methane to syngas. White boxes represent the coordination unsaturated Fe cations

the lattice oxygen. This catalyst exhibits a good stability with CO selectivity of around 95% and syngas production with H<sub>2</sub>/CO ratio of 2/1. A reversible transformation between homogeneous perovskite and oxides-encapsulated Fe<sup>0</sup> structures is identified during the reaction. Doping with Al greatly reduces the concentration of oxygen vacancies, which lowers the amount of active processes adsorbed oxygen. With these structure engineering processes, methane total combustion is suppressed and deep reduction of Fe cations from Fe<sup>4+</sup> to Fe<sup>0</sup> occurs without coke deposition, leading to better lattice oxygen donating ability, high CO selectivity, and stability of syngas production with ideal H<sub>2</sub>/CO ratio during long-term reaction process. On the other hand, this catalyst provides another source of syngas product when using CO<sub>2</sub> + H<sub>2</sub>O alternative to O<sub>2</sub> for recovery of the original structure. This perovskite material may be a promising catalyst system for practical application in solar-driven thermochemical process for syngas production by selective conversion of methane and H<sub>2</sub>O/CO<sub>2</sub> or other processes to avoid the carbon deposition.

## Methods

**Catalyst preparation.** To prepare La<sub>0.6</sub>Sr<sub>0.4</sub>Fe<sub>1-x</sub>Al<sub>x</sub>O<sub>3-δ</sub> ( $x = 0$  and  $0.2$ ) catalysts, stoichiometric La(NO<sub>3</sub>)<sub>3</sub>·6H<sub>2</sub>O, Sr(NO<sub>3</sub>)<sub>2</sub>, Fe(NO<sub>3</sub>)<sub>3</sub>·9H<sub>2</sub>O, and Al(NO<sub>3</sub>)<sub>3</sub>·9H<sub>2</sub>O were dissolved in deionized water under vigorous stirring to obtain a clear solution. Subsequently, citric acid (total metal ions/citric acid molar ratio = 1/2.5) was introduced to the solution, and the pH was adjusted to around 7 by dropwise adding of ammonia solution. The solution was concentrated to viscous gel at 80 °C. The gel was dried at 150 °C overnight, and then preheated to 450 °C for 4 h in air to remove organic species. After an intermediate grinding, the powders were further calcined at 1200 °C for 4 h in air to obtain the final La<sub>0.6</sub>Sr<sub>0.4</sub>Fe<sub>1-x</sub>Al<sub>x</sub>O<sub>3-δ</sub> catalysts. For comparison, LaFeO<sub>3</sub> catalyst was prepared following the same procedure. The difference is that the final LaFeO<sub>3</sub> material was obtained by calcination in air at 900 °C for 4 h to make its surface area comparable with that of LSAF6428 catalyst.

**Characterization.** The X-ray diffraction (XRD) patterns were recorded on a PANalytical X'Pert-Pro powder X-ray diffractometer (U = 40 KV, I = 40 mA) using Cu K<sub>α</sub> radiation. The lattice parameters of the catalysts were calculated based on all diffraction peaks. Brunauer–Emmett–Teller (BET) surface area of fresh catalysts was determined by nitrogen adsorption at -196 °C using a Quadrasorb SI instrument. The BET surface area of spent catalysts at 900 °C (reduction in 5% CH<sub>4</sub>/He and reoxidation in 5% O<sub>2</sub>/He) was measured by krypton adsorption at -196 °C using a TriStar 3020 instrument. XPS experiment was conducted on an ESCALAB 250 instrument equipped with a monochromatic Al K<sub>α</sub> source. The BE was calibrated using the adventitious carbon (C1s peak at 284.6 eV). The test of catalyst was quasi in situ conducted according to the following processes: first, it was first pretreated in CH<sub>4</sub> atmosphere at 900 °C and then cooled to room temperature in He atmosphere; after that the catalyst was moved to glovebox and ground to dense sheet, which was then transferred to the ESCALAB 250 instrument. Scanning electron microscopy (SEM) experiments were performed with a JEOL JSM-7800F electron microscope. The element distribution (line scan) was analyzed by transmission electron microscopy (TEM, JEOL JEM-2100F) equipped with energy dispersive X-ray spectroscopy (EDS) instrument. To gain insight into the internal structure of the reduced sample, the catalyst was further diced into thin films with the thickness of 50–100 nm. Before the cutting process, the catalyst particles were protected by a layer of epoxy to prevent from altering the

morphology of the thin films before it was observed by TEM. <sup>57</sup>Fe Mössbauer spectra were collected at room temperature using <sup>57</sup>Co γ-quantum source in the Rh matrix and the IS value was set with respect to that of α-Fe at room temperature. All spectra were computer-fitted by Lorentzian curves with a least squares fitting procedure.

The XAFS spectra at Fe K-edge of the catalysts were measured on beam line BL14W of the Shanghai Synchrotron Radiation Facility (China). A Si (111) double crystal monochromator was used and the energy was scanned from 200 eV below to 800 eV above the Fe K-edge (7112 eV). All spectra were measured in the transmission mode at room temperature.

**Performance tests.** The reaction of solar-driven partial oxidation of CH<sub>4</sub> was simulated in a quartz fixed-bed micro reactor packed with 100 mg (75–180 μm) catalyst at atmospheric pressure. In a typical experiment, the temperature was gradually increased to 900 °C in the flowing 5% O<sub>2</sub>/He atmosphere. After purged by He for 5 min, the selective oxidation of methane was started by injecting 5% CH<sub>4</sub>/He for 5 min. The lattice oxygen of the reduced catalysts was replenished by oxidation in 5% O<sub>2</sub>/He for 4 min. Between the oxidation and reduction process, the reactor was flushed with He to prevent mixing of CH<sub>4</sub> and O<sub>2</sub>. The total flow in the reactor was fixed to 30 mL/min. Twenty continuous cycles were performed for each sample, if not particularly stated. For LSAF6428 catalyst, the cycling stability was evaluated by 100 cycles. For experiment at 800 °C, the reduction time was prolonged to 7.5 min due to the relatively slow reaction rate while other conditions remain unchanged. To generate more syngas with H<sub>2</sub>/CO ratio of 2, a mixture of 2.5% CO<sub>2</sub> and 5% H<sub>2</sub>O balanced by He was used as oxidant alternative to O<sub>2</sub> while the oxidation time was adjusted to 3.5 min.

The reaction products were analyzed with an IPI GAM 200 quadrupole mass spectrometer system. The MS signals were calibrated before each experiment by using a calibration gas with known composition. The amount of all products (CO, CO<sub>2</sub>, and H<sub>2</sub>) and unreacted methane were calculated by integrating the MS signals of each species. The coke formation is calculated according to amount of CO and CO<sub>2</sub> produced during regeneration of the catalyst in oxygen atmosphere. The consumed methane and generated water in the reduction period were calculated from mass balance of C and H, respectively. The CO selectivity ( $S_{CO}$ ), converted lattice oxygen per gram catalyst ( $O_L$ ), and methane conversion ( $C_{CH_4}$ ) in each cycle were calculated as follows:

$$S_{CO} = \frac{n_{CO}}{n_{CO} + n_{CO_2} + n_{coke}} \times 100\% \quad (1)$$

$$O_L = \frac{n_{CO} + 2n_{CO_2} + n_{H_2O}}{0.1} \quad (2)$$

$$C_{CH_4} = \frac{n_{CO} + n_{CO_2} + n_{coke}}{n_{CH_4-U}} \times 100\% \quad (3)$$

$n_{CO}$ ,  $n_{CO_2}$ ,  $n_{coke}$ ,  $n_{H_2O}$  and  $n_{CH_4-U}$  represent the amount of CO, CO<sub>2</sub>, coke, H<sub>2</sub>O, and unreacted CH<sub>4</sub>, respectively.

The CH<sub>4</sub> pulse experiment was conducted on the Micromeritics Autochem 2920 apparatus. In a typical experiment, 200 mg catalyst loaded in a U-shape quartz tube. The catalyst was pre-heated to 900 °C in flowing air (20 mL/min), then the gas was changed to pure He (30 mL/min) to purge the air. Subsequently, pulses of 90% CH<sub>4</sub>/Ar were injected to the reactor with 1 min interval between two pulses. The tail gas was analyzed using an online mass spectrometer system.

**Computational details.** Density functional theory calculations were performed with the Vienna Ab Initio Simulation Package. The exchange correlation was

treated by the Perdew–Burke–Ernzerh generalized gradient approximation with spin-polarized functional. The projector-augmented wave method was used to describe the electron–core interaction, and the kinetic energy cutoff was set to be 450 eV. The DFT + U calculations were used to treat the on-site Coulomb and exchange interaction of the Fe d electrons with an effective  $U = 4.0$  eV. The  $\text{La}_{0.6}\text{Sr}_{0.4}\text{Fe}_{0.8}\text{Al}_{0.2}\text{O}_3$  (012) was modeled by ten atomic layers and the bottom-three layers were fixed, with a 15 Å vacuum between the slabs.

### Data availability

All data needed to evaluate the conclusions of this study are present in this article and the Supplementary Materials. Additional data related to this paper may be requested from the corresponding author.

Received: 18 April 2018 Accepted: 3 August 2018

Published online: 04 September 2018

### References

- Kodama, T. & Gokon, N. Thermochemical cycles for high-temperature solar hydrogen production. *Chem. Rev.* **107**, 4048–4077 (2007).
- Diver, R. B., Miller, J. E., Allendorf, M. D., Siegel, N. P. & Hogan, R. E. Solar thermochemical water-splitting ferrite-cycle heat engines. *J. Sol. Energy Eng.* **130**, 041001–041008 (2008).
- Lin, F., Rothensteiner, M., Alxniet, I., van Bokhoven, J. A. & Wokaun, A. First demonstration of direct hydrocarbon fuel production from water and carbon dioxide by solar-driven thermochemical cycles using rhodium–ceria. *Energy Environ. Sci.* **9**, 2400–2409 (2016).
- McDaniel, A. H. et al. Sr- and Mn-doped  $\text{LaAlO}_3$ -delta for solar thermochemical  $\text{H}_2$  and CO production. *Energy Environ. Sci.* **6**, 2424–2428 (2013).
- Marxer, D., Furler, P., Takacs, M. & Steinfeld, A. Solar thermochemical splitting of  $\text{CO}_2$  into separate streams of CO and  $\text{O}_2$  with high selectivity, stability, conversion, and efficiency. *Energy Environ. Sci.* **10**, 1142–1149 (2017).
- Palumbo, A. W., Sorli, J. C. & Weimer, A. W. High temperature thermochemical processing of biomass and methane for high conversion and selectivity to  $\text{H}_2$ -enriched syngas. *Appl. Energy* **157**, 13–24 (2015).
- Kodama, T., Shimizu, T., Satoh, T., Nakata, M. & Shimizu, K.-I. Stepwise production of CO-rich syngas and hydrogen via solar methane reforming by using a Ni (II)–ferrite redox system. *Sol. Energy* **73**, 363–374 (2002).
- Steinfeld, A., Frei, A., Kuhn, P. & Wuillemin, D. Solar thermal production of zinc and syngas via combined ZnO-reduction and  $\text{CH}_4$ -reforming processes. *Int. J. Hydrog. Energy* **20**, 793–804 (1995).
- Krenzke, P. T. & Davidson, J. H. Thermodynamic analysis of syngas production via the solar thermochemical cerium oxide redox cycle with methane-driven reduction. *Energy Fuels* **28**, 4088–4095 (2014).
- Choudhary, T. V. & Choudhary, V. R. Energy-efficient syngas production through catalytic oxy-methane reforming reactions. *Angew. Chem. Int. Ed.* **47**, 1828–1847 (2008).
- Scheffe, J. R. & Steinfeld, A. Oxygen exchange materials for solar thermochemical splitting of  $\text{H}_2\text{O}$  and  $\text{CO}_2$ : a review. *Mater. Today* **17**, 341–348 (2014).
- Arifin, D., Aston, V. J., Liang, X., McDaniel, A. H. & Weimer, A. W.  $\text{CoFe}_2\text{O}_4$  on a porous  $\text{Al}_2\text{O}_3$  nanostructure for solar thermochemical  $\text{CO}_2$  splitting. *Energy Environ. Sci.* **5**, 9438–9443 (2012).
- Steinfeld, A., Kuhn, P. & Karni, J. High-temperature solar thermochemistry: production of iron and synthesis gas by  $\text{Fe}_3\text{O}_4$ -reduction with methane. *Energy* **18**, 239–249 (1993).
- Go, K. S., Son, S. R., Kim, S. D., Kang, K. S. & Park, C. S. Hydrogen production from two-step steam methane reforming in a fluidized bed reactor. *Int. J. Hydrog. Energy* **34**, 1301–1309 (2009).
- Imtiaz, Q. et al. Development of  $\text{MgAl}_2\text{O}_4$ -stabilized, Cu-doped,  $\text{Fe}_2\text{O}_3$ -based oxygen carriers for thermochemical water-splitting. *J. Mater. Chem. A* **4**, 113–123 (2016).
- Li, K., Wang, H., Wei, Y. & Yan, D. Syngas production from methane and air via a redox process using Ce–Fe mixed oxides as oxygen carriers. *Appl. Catal. B* **97**, 361–372 (2010).
- Neal, L. M., Shafiearhoo, A. & Li, F. Dynamic methane partial oxidation using a  $\text{Fe}_2\text{O}_3$ @ $\text{La}_{0.8}\text{Sr}_{0.2}\text{FeO}_{3-\delta}$  core–shell redox catalyst in the absence of gaseous oxygen. *ACS Catal.* **4**, 3560–3569 (2014).
- Pena, M. A. & Fierro, J. L. G. Chemical structures and performance of perovskite oxides. *Chem. Rev.* **101**, 1981–2017 (2001).
- Mihai, O., Chen, D. & Holmen, A. Chemical looping methane partial oxidation: the effect of the crystal size and O content of  $\text{LaFeO}_3$ . *J. Catal.* **293**, 175–185 (2012).
- Mihai, O., Chen, D. & Holmen, A. Catalytic consequence of oxygen of lanthanum ferrite perovskite in chemical looping reforming of methane. *Ind. Eng. Chem. Res.* **50**, 2613–2621 (2011).
- Ryden, M. et al. Novel oxygen-carrier materials for chemical-looping combustion and chemical-looping reforming;  $\text{La}_x\text{Sr}_{1-x}\text{Fe}_y\text{Co}_{1-y}\text{O}_{3-\delta}$  perovskites and mixed-metal oxides of NiO,  $\text{Fe}_2\text{O}_3$  and  $\text{Mn}_3\text{O}_4$ . *Int. J. Greenh. Gas Control* **2**, 21–36 (2008).
- Haas, O. et al. The Fe K-edge X-ray absorption characteristics of  $\text{La}_{1-x}\text{Sr}_x\text{FeO}_{3-\delta}$  prepared by solid state reaction. *Mater. Res. Bull.* **44**, 1397–1404 (2009).
- Blasco, J. et al. Charge disproportionation in  $\text{La}_{1-x}\text{Sr}_x\text{FeO}_3$  probed by diffraction and spectroscopic experiments. *Phys. Rev. B Condens. Matter* **77**, 054107 (2008).
- Hu, R. et al. Photocatalytic activities of  $\text{LaFeO}_3$  and  $\text{La}_3\text{FeTiO}_6$  in p-chlorophenol degradation under visible light. *Catal. Commun.* **29**, 35–39 (2012).
- Yang, J. et al. Crystal structure, magnetic properties, and Mössbauer studies of  $\text{La}_{0.6}\text{Sr}_{0.4}\text{FeO}_{3-\delta}$  prepared by quenching in different atmospheres. *Phys. Rev. B Condens. Matter* **66**, 184415 (2002).
- Shimony, U. & Knudsen, J. M. Mössbauer studies on iron in the perovskites  $\text{La}_{1-x}\text{Sr}_x\text{FeO}_3$  ( $0 \leq x \leq 1$ ). *Biophys. Rev.* **144**, 361–366 (1966).
- Rida, K., Benabbas, A., Bouremmad, F., Peña, M. A. & Martínez-Arias, A. Surface properties and catalytic performance of  $\text{La}_{1-x}\text{Sr}_x\text{CrO}_3$  perovskite-type oxides for CO and  $\text{C}_3\text{H}_6$  combustion. *Catal. Commun.* **7**, 963–968 (2006).
- Ponce, S., Peña, M. A. & Fierro, J. L. G. Surface properties and catalytic performance in methane combustion of Sr-substituted lanthanum manganites. *Appl. Catal. B* **24**, 193–205 (2000).
- Wang, Y. et al. Nanocasted synthesis of mesoporous  $\text{LaCoO}_3$  perovskite with extremely high surface area and excellent activity in methane combustion. *J. Phys. Chem. C* **112**, 15293–15298 (2008).
- Dai, X. P., Wu, Q., Li, R. J., Yu, C. C. & Hao, Z. P. Hydrogen production from a combination of the water–gas shift and redox cycle process of methane partial oxidation via lattice oxygen over  $\text{LaFeO}_3$  perovskite catalyst. *J. Phys. Chem. B* **110**, 25856–25862 (2006).
- Zafar, Q., Mattisson, T. & Gevert, B. Integrated hydrogen and power production with  $\text{CO}_2$  capture using chemical-looping reforming redox reactivity of particles of CuO,  $\text{Mn}_2\text{O}_3$ , NiO, and  $\text{Fe}_2\text{O}_3$  using  $\text{SiO}_2$  as a support. *Ind. Eng. Chem. Res.* **44**, 3485–3496 (2005).
- Ryden, M., Johansson, M., Lyngfelt, A. & Mattisson, T. NiO supported on Mg–ZrO<sub>2</sub> as oxygen carrier for chemical-looping combustion and chemical-looping reforming. *Energy Environ. Sci.* **2**, 970–981 (2009).
- Nakayama, O., Ikenaga, N.-o., Miyake, T., Yagasaki, E. & Suzuki, T. Partial oxidation of  $\text{CH}_4$  with air to produce pure hydrogen and syngas. *Catal. Today* **138**, 141–146 (2008).
- He, F., Trainham, J., Parsons, G., Newman, J. S. & Li, F. A hybrid solar-redox scheme for liquid fuel and hydrogen coproduction. *Energy Environ. Sci.* **7**, 2033–2042 (2014).
- Luo, S. et al. Shale gas-to-syngas chemical looping process for stable shale gas conversion to high purity syngas with a  $\text{H}_2$ :CO ratio of 2:1. *Energy Environ. Sci.* **7**, 4104–4117 (2014).
- Pralhad, H. V., Feng, H., Amit, M. & Fanxing, L. Iron-doped  $\text{BaMnO}_3$  for hybrid water splitting and syngas generation. *ChemSusChem* **10**, 3402–3408 (2017).
- Zhang, J., Haribal, V. & Li, F. Perovskite nanocomposites as effective  $\text{CO}_2$ -splitting agents in a cyclic redox scheme. *Sci. Adv.* **3**, e1701184 (2017).
- He, F. et al. The use of  $\text{La}_{1-x}\text{Sr}_x\text{FeO}_3$  perovskite-type oxides as oxygen carriers in chemical-looping reforming of methane. *Fuel* **108**, 465–473 (2013).
- Huang, C. et al. Sn promoted  $\text{BaFeO}_{3-\delta}$  catalysts for  $\text{N}_2\text{O}$  decomposition: optimization of Fe active centers. *J. Catal.* **347**, 9–20 (2017).
- Tsvetkov, N., Lu, Q., Sun, L., Crumlin, E. J. & Yildiz, B. Improved chemical and electrochemical stability of perovskite oxides with less reducible cations at the surface. *Nat. Mater.* **15**, 1010–1016 (2016).
- Christian Enger, B., Lødeng, R. & Holmen, A. A review of catalytic partial oxidation of methane to synthesis gas with emphasis on reaction mechanisms over transition metal catalysts. *Appl. Catal. A* **346**, 1–27 (2008).
- Tauster, S., Fung, S. & Garten, R. L. Strong metal-support interactions. Group 8 noble metals supported on titanium dioxide. *J. Am. Chem. Soc.* **100**, 170–175 (1978).
- Liu, X. et al. Strong metal–support interactions between gold nanoparticles and ZnO nanorods in CO oxidation. *J. Am. Chem. Soc.* **134**, 10251–10258 (2012).
- Mohaddes-Ardabili, L. et al. Self-assembled single-crystal ferromagnetic iron nanowires formed by decomposition. *Nat. Mater.* **3**, 533–538 (2004).
- Li, W., Zhu, X., Chen, S., Yang, W. Integration of nine steps into one membrane reactor to produce synthesis gases for ammonia and liquid fuel. *Angew. Chem. Int. Ed.* **55**, 8566–8570 (2016).
- Ivanov, D. V. et al. Effect of surface decoration with  $\text{LaSrFeO}_4$  on oxygen mobility and catalytic activity of  $\text{La}_{0.4}\text{Sr}_{0.6}\text{FeO}_{3-\delta}$  in high-temperature  $\text{N}_2\text{O}$

- decomposition, methane combustion and ammonia oxidation. *Appl. Catal. A* **457**, 42–51 (2013).
47. Huang, C. et al. Preparation of  $\text{BaSnO}_3$  and  $\text{Ba}_{0.96}\text{La}_{0.04}\text{SnO}_3$  by reactive core-shell precursor: formation process, CO sensitivity, electronic and optical properties analysis. *RSC Adv.* **6**, 25379–25387 (2016).
48. Buscaglia, M. T., Buscaglia, V. & Alessio, R. Coating of  $\text{BaCO}_3$  crystals with  $\text{TiO}_2$ : versatile approach to the synthesis of  $\text{BaTiO}_3$  tetragonal nanoparticles. *Chem. Mater.* **19**, 711–718 (2007).

### Acknowledgements

This work was supported by National Key Projects for Fundamental Research and Development of China (2016YFA0202801) and National Natural Science Foundation of China (21706254, 21676269, 21576251, 21406225, 91645023, 21603170). The authors thank Yang Su and Yujing Ren for fruitful discussions and support on TEM experiments. The calculations were performed by using the HPC Platform at National Super-computing Center in Shenzhen.

### Author contributions

C.D.H. performed the catalyst preparation, characterizations, catalytic tests, and paper writing. J.L. and X.D.W. conceived the research and co-wrote this manuscript. J.W. helped the catalyst preparation and characterizations. Y.T.C. and C.R.C. conducted DFT calculations and wrote part of the paper (calculation). M.T. and A.Q.W. helped to discuss the performance results. A.I.R. and J.H.W. helped to analyze the  $^{57}\text{Fe}$  Mössbauer results. B.L.H. performed the thermodynamic analysis. X.L.P. conducted the STEM examinations and helped the result analysis. All authors contributed to the critical discussions of the manuscript.

### Additional information

**Supplementary Information** accompanies this paper at <https://doi.org/10.1038/s42004-018-0050-y>.

**Competing interests:** The authors declare no competing interests.

**Reprints and permission** information is available online at <http://npg.nature.com/reprintsandpermissions/>

**Publisher's note:** Springer Nature remains neutral with regard to jurisdictional claims in published maps and institutional affiliations.



**Open Access** This article is licensed under a Creative Commons Attribution 4.0 International License, which permits use, sharing, adaptation, distribution and reproduction in any medium or format, as long as you give appropriate credit to the original author(s) and the source, provide a link to the Creative Commons license, and indicate if changes were made. The images or other third party material in this article are included in the article's Creative Commons license, unless indicated otherwise in a credit line to the material. If material is not included in the article's Creative Commons license and your intended use is not permitted by statutory regulation or exceeds the permitted use, you will need to obtain permission directly from the copyright holder. To view a copy of this license, visit <http://creativecommons.org/licenses/by/4.0/>.

© The Author(s) 2018